

Magnetic modelling and tomography: First steps towards a consistent reconstruction of the solar corona

T. Wiegelmann (wiegelmann@linmpi.mpg.de) and B. Inhester
*Max-Planck-Institut für Aeronomie, Max-Planck-Strasse 2, 37191
Katlenburg-Lindau, Germany*

DOI: 10.1023/A:1024282131117
Bibliographic Code: 2003SoPh..214..287W

Abstract. We undertake a first attempt towards a consistent reconstruction of the coronal magnetic field and the coronal density structure. We consider a stationary solar corona which has to obey the equations of magnetohydrostatics. We solve these equations with help of a newly developed optimization scheme. As a first step we illustrate how tomographic information can be included into the reconstruction of coronal magnetic fields. In a second step we use coronal magnetic field information to improve the tomographic inversion process. As input the scheme requires magnetic field measurements on the photosphere from vector-magnetographs and the line-of-sight integrated density distribution from coronagraphs. We test our codes with well known analytic magnetohydrostatic equilibria and models. The program is planned for use within the STEREO mission.

Keywords: Tomography, MHD, Coronal magnetic fields, Stereo

Abbreviations: KAP – Kluwer Academic Publishers; compuscript – Electronically submitted article

JEL codes: D24, L60, 047

Nomenclature:

KAP – Kluwer Academic Publishers; compuscript – Electronically submitted article

1. Introduction

The solar magnetic field is an important quantity which couples the solar interior, the photosphere and the atmosphere. The quasi stationary coronal magnetic field configuration is an interesting and challenging topic on its own right. But even to understand basic processes like coronal mass ejections and flares it is important to understand the quiescent magnetic configuration out of which these dynamic phenomena arise. Unfortunately the coronal magnetic field cannot be measured directly, but it has to be reconstructed from photospheric measurements. A magnetic field reconstruction of the solar corona has to be consistent with



© 2008 Kluwer Academic Publishers. Printed in the Netherlands.

the observed spatial variation of the coronal plasma (density, pressure, temperature) often elongated along the magnetic field.

Here we are mainly interested in long living structures which are time independent in first order. We also concentrate on closed magnetic configuration where a stationary plasma flow (solarwind) does not significantly contribute to the force balance. Such configurations are static equilibria and have to obey the magnetohydrostatic equations (MHS).

As the magnetic field \mathbf{B} and the density distribution N are physically closely related their model reconstruction should also be linked as much as possible. In this paper we attempt to show how this can be achieved. We propose variational principles which if they can be solved should give a consistent model for an isothermal corona. For the magnetic field reconstruction this leads to a generalization of a nonlinear force-free approach by (Wheatland et al., 2000), for the density reconstruction we obtain a tomography problem with an improved regularization term.

The ground based or space-born magnetograph observation provide either the line-of-sight magnetic field (B_{los} , e.g. MDI on SOHO), which is sufficient for potential and linear force-free fields, or all three components of the photospheric magnetic field (e.g. IVM in Hawaii, expected also from SolarB). The latter information is sufficient to determine nonlinear force-free fields completely. As a force-free approximation is justified only in the limit of a vanishing plasma β , we take into account forces (pressure gradient and gravity) for configurations with a finite plasma β even though we shall consider β small.

Popular simplifications for the reconstruction of coronal magnetic fields are:

- Potential fields ($\mathbf{j} = \mathbf{0}$) (e.g. Schmidt, 1964; Semel, 1967; Schatten, Wilcox, and Ness, 1969; Sakurai, 1982; Rudenko, 2001a)
- Linear force-free fields (e.g. Nakagawa and Raadu, 1972; Chiu and Hilton, 1977; Seehafer, 1978; Semel, 1988; Gary, 1989; Lothian and Browning, 1995)
- Linear non force-free fields (e.g. Zhao and Hoeksema, 1993; Zhao and Hoeksema, 1994; Petrie and Neukirch, 2000; Zhao, Hoeksema, and Scherrer, 2000; Rudenko, 2001b)
- Nonlinear force-free fields (e.g. Sakurai, 1981; Wu, Chang, and Hagyard, 1985; Roumeliotis, 1996; Amari et al., 1997; McClymont, Jiao, and Mikic, 1997; Wheatland et al., 2000; Yan and Sakurai, 2000).

Within this work we do not use any of these assumptions but consider the general case of nonlinear non-force-free equilibria. The mathematical problem of calculating nonlinear non-force-free fields is closely

related to the problem of calculating nonlinear force-free fields which coincides with the above in the limit of $\beta \rightarrow 0$. Under ideal conditions the information contained in a (perfect) vectormagnetogram together with the force-free condition would be sufficient to calculate the coronal magnetic field. Within this work we show that the information contained in a vectormagnetogram together with a tomographic reconstructed coronal density distribution and the assumption of magnetohydrostatic force balance is as well sufficient to calculate the finite β coronal magnetic field. Unfortunately current vectormagnetograms and tomographic reconstruction are far from being perfect, which affects the quality of reconstruction. Within this work we use well known MHS-equilibria to test our newly developed reconstruction program. The use of analytic equilibria as artificial data allows us to extract ideal vectormagnetograms as well as ideal coronal density distributions.

As for the density observations, ground based coronagraphs (e.g., the Mark III coronagraph on Hawaii, LASCO coronagraph on SOHO and the future STEREO mission) provide the line of sight integrated density structure of the solar corona from different relative viewpoints as the Sun rotates. These measurements have been used for a 3D-reconstruction of the coronal plasma distribution with help of tomographic methods (Davila, 1994; Zidowitz, 1999; Frazin, 2000; Frazin, 2002). The major problems here are:

- the assumption of stationarity of coronal structures as the Sun rotates,
- the lack of data due to the occulted center of the image,
- the nonideal viewing geometry caused by a slight tilt of the Sun's axis with respect to the ecliptic.

These shortcomings generally enhance the intrinsic ill-posedness of the tomography problem. The general approach to stabilize the reconstruction is to smooth the solution by regularization. The prize to pay is a reduced spatial resolution of the model depending on the quality of the data and inconsistencies and ill-conditioning due to the above effects. So far only very general, isotropic regularization operators have been applied to coronal density reconstruction problems. Our approach to the density reconstruction in connection with the reconstruction of the coronal magnetic field leads to a new regularization operator which, as we demonstrate by test calculations, could yield a better spatial resolution than conventional reconstructions.

The paper is outlined as follows. In section 2 we describe the basic equations and the newly developed algorithm of the magnetic field reconstruction program in the case where the plasma density distribution

N is given. Section 3 contains several test-runs where we apply our code for the reconstruction of analytic MHS-equilibria. In section 4 we propose an algorithm for an improved reconstruction of N if some information of \mathbf{B} is given. This approach is tested and compared with conventional methods by with the help of a two dimensional analytic coronal density distribution. In the final section 5 we discuss how both methods could be used together to derive a consistent model of the Sun's corona. In appendix A, B and C we provide the algebra which has been omitted in the text.

2. Basic equations

We describe the coronal plasma with help of the magnetohydro static (MHS) equations. The MHS equations are

$$\mathbf{j} \times \mathbf{B} - \nabla P - \rho \nabla \Psi = \mathbf{0}, \quad (1)$$

$$\nabla \times \mathbf{B} = \mu_0 \mathbf{j}, \quad (2)$$

$$\nabla \cdot \mathbf{B} = 0, \quad (3)$$

where \mathbf{B} is the magnetic field, \mathbf{j} the electric current density, P the plasma pressure, ρ the plasma density, μ_0 the vacuum permeability and Ψ the solar gravity potential. We define the functional

$$L = \int_V \left[B^{-2} |(\nabla \times \mathbf{B}) \times \mathbf{B} - \mu_0(\nabla P + \rho \nabla \Psi)|^2 + |\nabla \cdot \mathbf{B}|^2 \right] d^3x. \quad (4)$$

The domain V is a volume which on one side is bounded by the sun's photosphere. Obviously, L is bound from below by 0. This bound is attained if the magnetic field satisfies the MHS equations. Here we assume that the plasma pressure and the density are given. It is assumed that the corresponding information will be provided by tomographic reconstruction of the solar corona. We vary functional L with respect to an iteration parameter t and get (see Appendix A for the derivation)

$$\frac{1}{2} \frac{dL}{dt} = - \int_V \frac{\partial \mathbf{B}}{\partial t} \cdot \mathbf{F} d^3x - \int_S \frac{\partial \mathbf{B}}{\partial t} \cdot \mathbf{G} d^2x, \quad (5)$$

where

$$\begin{aligned} \mathbf{F} = & \nabla \times (\boldsymbol{\Omega}_a \times \mathbf{B}) - \boldsymbol{\Omega}_a \times (\nabla \times \mathbf{B}) \\ & + \nabla(\boldsymbol{\Omega}_b \cdot \mathbf{B}) - \boldsymbol{\Omega}_b(\nabla \cdot \mathbf{B}) + (\boldsymbol{\Omega}_a^2 + \boldsymbol{\Omega}_b^2) \mathbf{B}, \end{aligned} \quad (6)$$

$$\mathbf{G} = \hat{\mathbf{n}} \times (\boldsymbol{\Omega}_a \times \mathbf{B}) - \hat{\mathbf{n}}(\boldsymbol{\Omega}_b \cdot \mathbf{B}), \quad (7)$$

$$\begin{aligned}\boldsymbol{\Omega}_{\mathbf{a}} &= B^{-2} [(\nabla \times \mathbf{B}) \times \mathbf{B} - \mu_0(\nabla P + \rho \nabla \Psi)], \\ \boldsymbol{\Omega}_{\mathbf{b}} &= B^{-2} [(\nabla \cdot \mathbf{B}) \mathbf{B}].\end{aligned}\tag{8}$$

The surface integral in (5) vanishes if \mathbf{B} is prescribed on the boundary. We iterate the magnetic field inside the computational box with

$$\frac{\partial \mathbf{B}}{\partial t} = \mu \mathbf{F},\tag{9}$$

which ensures that L is monotonously decreasing. For the bottom the boundary values are given by the photospheric vector magnetograph observations. On other boundaries we may either assume \mathbf{B} or include the boundary values in the variation. Actually the handling of the not observed lateral and top boundaries of the computational box is similar here as in the nonlinear force-free case (Wiegelmann and Neukirch, 2003). On the boundary of the computational box the magnetic field is iterated with

$$\frac{\partial \mathbf{B}}{\partial t} = 0 \quad \text{where } \mathbf{B} \text{ observed},\tag{10}$$

$$\frac{\partial \mathbf{B}}{\partial t} = \mu \mathbf{G} \quad \text{else}.\tag{11}$$

We propose to use this iteration process to solve for the minimum of L . If a solution of the MHS-equations for the prescribed boundary condition exist, the global minimum of L corresponds to this solution and attains $L = 0$. Please note that the iteration procedure ensures to find this global minimum if the solution space is convex. For a non convex solution space it is possible that the iteration will lead to a local minimum. For complicated magnetic field configurations it is difficult to decide in advance whether the solution space is convex or not. For a non convex solution space it is still possible to find the global minimum by iteration if the start configuration is sufficient close (within a convex area) to this minimum. The method generalizes an approach by (Wheatland et al., 2000) which has been used to compute force-free fields.

3. Convergence Tests

Since analytic truly 3D MHS equilibria are not available, we use an analytic 2D MHS-equilibrium to test the newly developed code. The analytic equilibria are not meant to be a good representation of the solar corona and the tests are only carried out to check the convergence

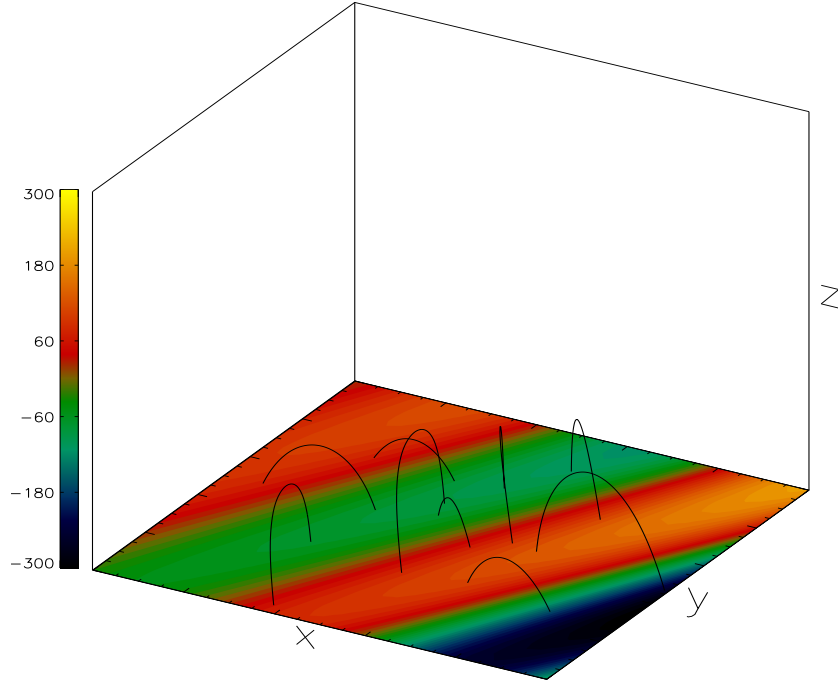


Figure 1. MHS-1: Some field lines for the first equilibrium. The colours on the photosphere correspond to the normal component of the magnetic field.

of the newly developed code. We represent the magnetic field with help of the flux-function $A(x, z)$ as

$$\mathbf{B} = \nabla A \times \mathbf{e}_y + B_y \mathbf{e}_y \quad (12)$$

and the MHS equations reduce to a Grad-Shafranov equation

$$-\Delta A = \frac{\partial}{\partial A} \left(P(A, \Psi) + \frac{B_y^2(A)}{2} \right). \quad (13)$$

3.1. EQUILIBRIUM MHS-1

As a first test we consider equilibria without gravity ($P = P(A)$) and choose $P(A) \propto A^2$ and $B_y(A) \propto A$. The corresponding Grad-Shafranov equation is linear in A and can be solved analytically by a separation ansatz. It is convenient to define a function

$$\Pi(A) = c^2 A^2 = P(A) + \frac{B_y^2(A)}{2}, \quad (14)$$

$$P(A) = a_0 c^2 A^2, \quad (15)$$

$$B_y(A) = \sqrt{(1 - a_0) c} A. \quad (16)$$

Configurations with $c = 0$ correspond to potential fields, finite c and $a_0 = 0$ to force-free equilibria, $a_0 = 1$ to equilibria with pressure gradient but without magnetic shear and finally $0 < a_0 < 1$ is the general case including both forces and magnetic shear. With this approach we get the solution of (13):

$$A(x, z) = \sum_{k=1}^{\infty} \exp(-\nu \pi z / L) [a_k \cos(k \pi x / L) + b_k \sin(k \pi x / L)], \quad (17)$$

where $\nu = \sqrt{k^2 - c^2}$, for $c^2 < k^2$. The solutions of the Grad-Shafranov equation are invariant in one spatial coordinate ($\frac{\partial}{\partial y} = 0$). To test our 3D-optimization code it would be more convenient to have equilibria varying in all three spatial directions. We construct such equilibria by rotating the solution of Grad Shafranov equation by an angle ϕ_1 around the z -axis and by ϕ_2 around the y -axis. As a result the solution varies in all of our three coordinate directions. The final equilibrium has the following free parameters: $c, a_0, a_k, b_k, \phi_1, \phi_2$. As an example we choose ($c = 0.8, a_0 = 0.5, a_1 = 1.0, a_3 = -0.8, a_k = b_k = 0$ for all other $k, \phi_1 = -0.05\pi, \phi_2 = 0.15\pi$.) With help of the flux function (17), the equations for the pressure (15), shear field (16) and the magnetic field definition (12) we get the magnetic field \mathbf{B} and the plasma pressure P . For an isothermal plasma we derive the density as $\rho = \frac{P}{RT}$. We normalize the maximum normal magnetic field at $z = 0$ to 300 Gauss = 0.03 T.

As a first test, we want to reconstruct this equilibrium with our code. The code needs any 3D-vector field as start configuration for the iteration procedure and it is convenient to choose a potential magnetic field with respect to the photospheric line of sight magnetic field. The potential field can be easily computed for an observed magnetogram. For our model data a potential field is computed with the same parameter set but $c = 0$. The boundary values for the iteration are in practical cases only known on the bottom plane. On the others plans they have to be iterated too using (11). In this test we fix the magnetic field however everywhere on the boundary to the value of the analytic solution to simplify the problem. For the force-free case we treated the side and top boundaries as unknowns in (Wiegelmann and Neukirch, 2003) and showed how they can be iteratively determined by (11). This latter way of treating the boundary values makes the finding of a solution much more difficult.

In figure 1 we show three-dimensional plots of selected field lines for this MHS-equilibrium. The colour coding of the bottom boundary

indicates the distribution of B_n on that boundary. To test our code we try to reconstruct that equilibrium in the following way:

- Inside the computational box we choose a potential magnetic field as start equilibrium.
- We prescribe the plasma pressure in the box with the analytic solution.
- We prescribe the vector magnetic field on the boundaries of the computational box.
- We iterate for the magnetic field inside the computational box with (9).

During the computations we calculate the quantities L , the absolute value of the force balance $|\mathbf{J} \times \mathbf{B} - \nabla P|$ (averaged over the numerical grid), the value of $|\nabla \cdot \mathbf{B}|$ (averaged over the numerical grid), and the difference between the numerical magnetic field and the known analytical solution $|\mathbf{B}(t) - \mathbf{B}_{\text{ana}}|^2 / |\mathbf{B}_{\text{ana}}|^2$ (averaged over the numerical grid) at each time step. In figure 2 we show the development of these quantities during the iteration process with logarithmic scaling. All quantities decrease over several orders of magnitude during the optimization process and reach the level of the discretisation error. The discretisation error corresponds to the value of L , $|\mathbf{J} \times \mathbf{B} - \nabla P - \rho \nabla \Psi|$ and $|\nabla \cdot \mathbf{B}|$ for the analytic solution computed on a numerical grid. In the upper half of table I we summarize the main result of the iteration process. The first row corresponds to the analytic solution computed on a grid and defines the discretisation error. The second row contains the values of L , the force balance and the relative error for the start configuration, where the interior points have been replaced by a potential field. The relatively large values of the three quantities are due to the deviation from the equilibrium. The next rows show how the three diagnostic quantities evolve during the iteration. After 10000 iteration-steps the discretisation error is reached for all values and the original equilibrium MHS-1 has been reconstructed.

We use a Landweber iteration (see e.g. (Louis, 1989)) with some automatic control of the stepsize. The continuous form of equation (9) ensures a monotonously decreasing L . A monotonously decreasing L in the discretized form is ensured if the iteration step dt is sufficiently small. The code checks if $L(t + dt) < L(t)$ after each time step and if the condition is not fulfilled, the iteration step is refused and dt is reduced by a factor of 2. After each successful iteration step we increase dt slowly by a factor of 1.01 to allow the time step to become as large as possible with respect to the stability condition. In principle

Table I. Details of runs to reconstruct MHS equilibria.

$n_x \times n_y \times n_z$	Step	$\frac{L}{[T^2 m]}$	$\frac{\text{Force} - \text{balance}}{[\text{nN m}^{-3}]}$	Relative Error
$40 \times 40 \times 20$ Start	MHS-1	0.0028	0.19	Reference
	0	140613	1205	0.27
	500	74	25.5	0.025
	5000	0.021	0.4	$1.4 \cdot 10^{-5}$
	10000	0.0028	0.19	$< 10^{-6}$
$40 \times 40 \times 200$ Start	MHS-2	4.3	10.7	Reference
	0	$3.7 \cdot 10^7$	15290	0.14
	500	101423	2399	0.017
	1000	3393	430	$9 \cdot 10^{-4}$
	5000	4.3	10.8	$< 10^{-6}$

there are more sophisticated methods available to calculate an effective dt for each iteration step (see e.g. (Geiger and Kanzow, 1999)) but these methods have a huge numerical overhead and further numerical experiments will have to show which of these are favourable for our problem.

3.2. EQUILIBRIUM MHS-2, HELMET STREAMER

As a second example we consider an equilibrium with gravity which has been used to model coronal helmet streamers (Wiegelmann et al., 1998). The method is based on the asymptotic expansion method (Schindler, 1972) and corresponds to a nonlinear Grad-Shafranov equation. Here we choose for the terms in (13)

$$P(A, \Psi) = a_0 \exp\left(-\frac{\Psi}{RT}\right) \exp(c A), \quad (18)$$

$$B_y(A) = 2 \sqrt{1 - a_0} \exp\left(\frac{c}{2} A\right). \quad (19)$$

For simplicity we use a constant gravity $\Psi = g z$, $g = 270 \frac{\text{m}}{\text{s}^2}$ and a constant coronal temperature $T = 3 \cdot 10^6 \text{ K}$. Consequently we get the mass density from the plasma pressure as $\rho = P/RT$. The parameters correspond to a coronal pressure scale height

$$H_0 = \frac{k_B T}{m |\nabla \Psi|} = \frac{RT}{g} \quad (20)$$

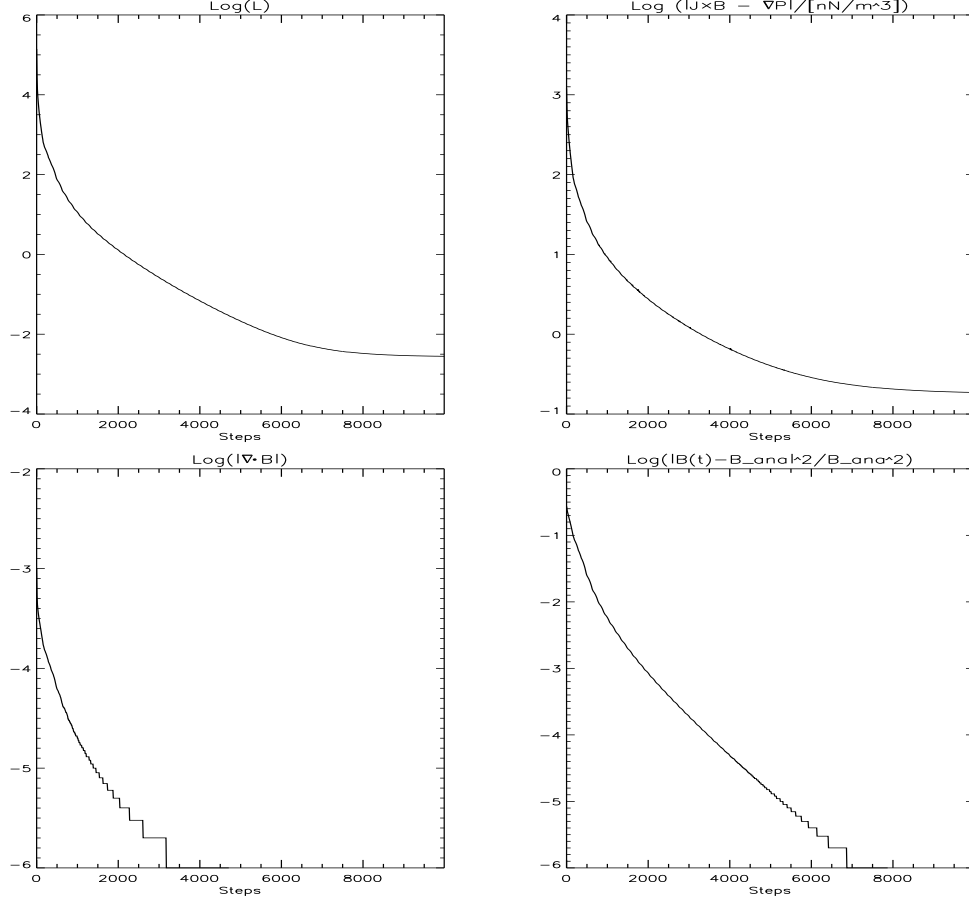


Figure 2. MHS-1: Evolution of L , force balance $|\mathbf{j} \times \mathbf{B} - \nabla P|$, $|\nabla \cdot \mathbf{B}|$ and the difference between the numerical magnetic field and the known analytical solution $|\mathbf{B}(t) - \mathbf{B}_{\text{ana}}|^2 / |\mathbf{B}_{\text{ana}}|^2$. All quantities are averaged over the numerical grid.

of $93 \text{ Mm} \approx 0.13$ solar radii. With help of the method of asymptotic expansion we find an analytic solution of (13):

$$A(x, z) = -\frac{2}{c} \log \left(\cosh \left(c \sqrt{\frac{p_0(z)}{2}} x \right) \right) + \frac{1}{c} \log \left(\frac{p_0(z)}{k_0(z)} \right), \quad (21)$$

$$p_0(z) = \frac{1}{1 + \lambda z}, \quad (22)$$

$$k_0(z) = \exp \left(-\frac{\Psi}{RT} \right) = \exp \left(-\frac{z}{H_0} \right). \quad (23)$$

We choose $c = 0.05 \text{ Mm}^{-1}$ and $\lambda = 0.001 \text{ Mm}^{-1}$ for the free parameters and compute the solution on a grid of $nx = ny = 40$, $nz = 200$. With

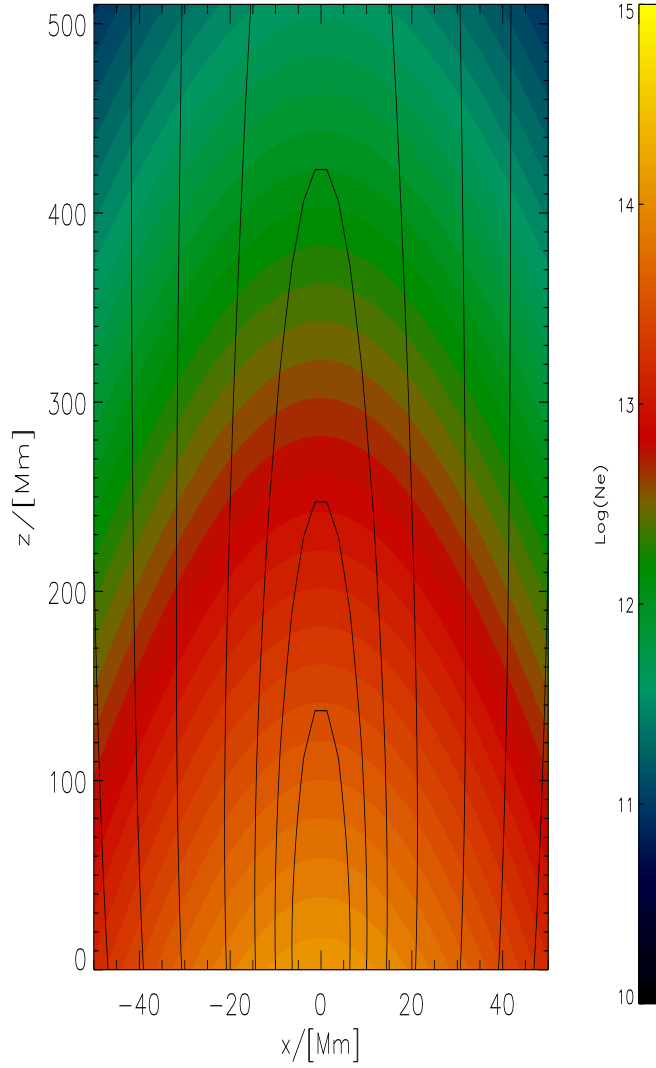


Figure 3. MHS 2: A projection of some field lines for MHS-2. The back ground colours correspond to the logarithm of the electron number density $\frac{N}{[m^3]}$. Please note the different scale in x and z.

help of the flux function (21), the equations for the pressure (18), shear field (19) and the magnetic field definition (12) we get the magnetic field \mathbf{B} and the plasma pressure P . For an isothermal plasma we derive the number density as $N = \frac{P}{k_B T}$. Let us remark that the quantity N is what we will get for real data from coronal measurements after the tomographic reconstruction. In principle a non-constant temperature

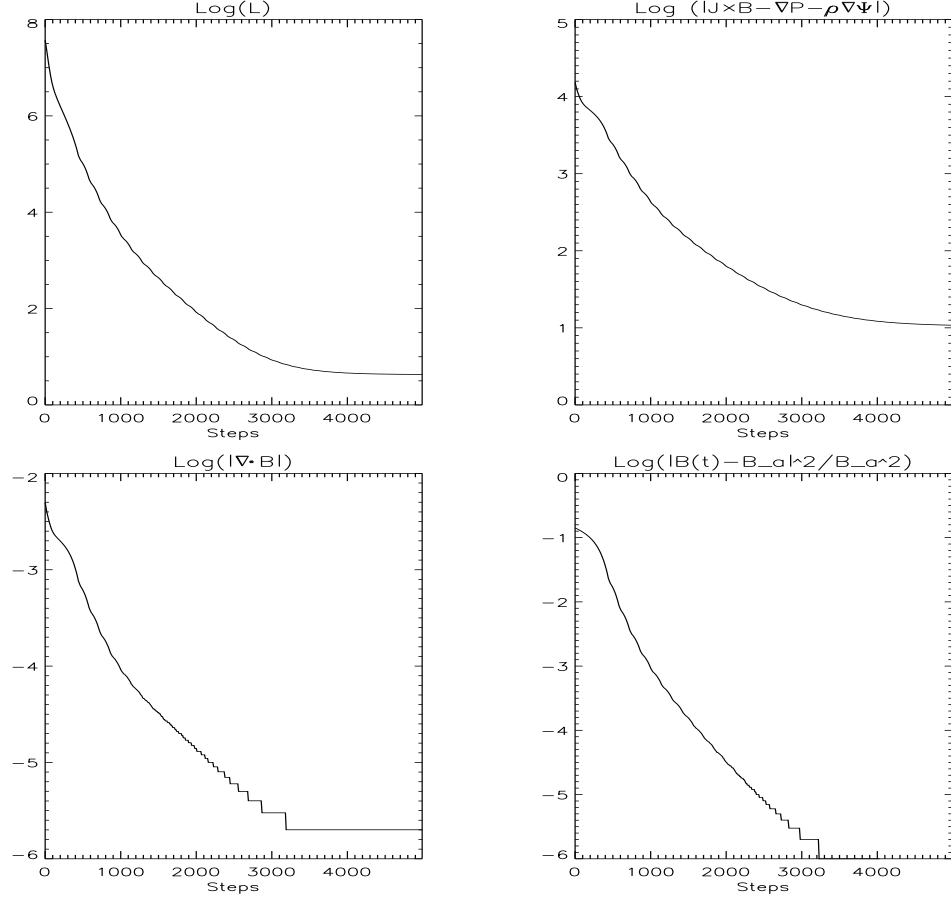


Figure 4. MHS-2: Evolution of L , force balance $|\mathbf{j} \times \mathbf{B} - \nabla P - \rho \nabla \Psi|$, $|\nabla \cdot \mathbf{B}|$ and the difference between the numerical magnetic field and the known analytical solution $|\mathbf{B}(t) - \mathbf{B}_{\text{ana}}|^2 / |\mathbf{B}_{\text{ana}}|^2$. All quantities are averaged over the numerical grid.

T can also be used, e.g. from a standard atmosphere model. Figure 3 shows a projection of magnetic field lines and the electron density structure as background for the helmet streamer configuration MHS-2.

The solution is invariant in y and we rotate the solution around the z -axis with an angle $\phi = \pi/10$ which is useful for testing our reconstruction code (All derivatives appear). As start magnetic field we choose a Harris-sheet, where the magnetic field has only one component $B_z = -\sqrt{2} \tanh\left(\frac{c}{\sqrt{2}} x\right)$ which is invariant in z and y . We apply our code for the reconstruction of this helmet streamer equilibrium MHS-2 in the following way:

- Inside the computational box we choose a Harris-sheet magnetic field as start equilibrium.
- We prescribe the electron number density N in the box with the analytic solution.
- Under the assumption of a constant coronal temperature and a constant gravity we calculate the plasma pressure, density and compute $\mathbf{u} = -\mu_0(\nabla P + \rho \nabla \Psi)$ on the grid.
- We prescribe the vector magnetic field on the boundaries of the computational box. Similar as in the previous example we use the analytic solution to fix the magnetic field on all boundaries for simplicity.
- We iterate for the magnetic field inside the computational box with (9).

Similar as for MHS-1 we diagnose the quantities L , the absolute value of the force balance $|\mathbf{J} \times \mathbf{B} - \nabla P - \rho \nabla \Psi|$ (averaged over the numerical grid), the value of $|\nabla \cdot \mathbf{B}|$ (averaged over the numerical grid), and the difference between the numerical magnetic field and the known analytical solution $|\mathbf{B}(t) - \mathbf{B}_{\text{ana}}|^2 / |\mathbf{B}_{\text{ana}}|^2$ (averaged over the numerical grid) at each time step. In figure 4 we show the development of these quantities during the iteration process with logarithmic scaling. All quantities decrease over several orders of magnitude during the optimization process and reach the level of the discretisation error. The discretisation error corresponds to the value of L , $|\mathbf{J} \times \mathbf{B} - \nabla P - \rho \nabla \Psi|$ and $|\nabla \cdot \mathbf{B}|$ for the analytic solution computed on a numerical grid. Please note that the discretisation error for MHS-2 is significantly larger as for MHS-1 due to the nature of nonlinear analytic solution. In the lower half of table I we summarize the main result of the iteration process.

The first row corresponds to the analytic solution computed on a grid and defines the discretisation error. The second row contains the values of L , the force balance and the relative error for the start configuration, where the interior points have been replaced by a Harris-sheet magnetic field. The large values of the three quantities are due to the deviation from the equilibrium. The next rows show how the three diagnostic quantities evolve during the iteration. After 5000 iteration-steps the discretisation error is reached for all values and the original helmet streamer-configuration MHS-2 has been reconstructed.

3.3. FORCE-FREE AND MHS RECONSTRUCTION FOR DIFFERENT β

It is generally assumed that the magnetic pressure in the lower corona is much larger than the plasma pressure leading to $\beta \ll 1$. For longer structures like helmet streamers the plasma β increases significantly. It is generally assumed that the effects of plasma pressure and gravity can be neglected for low β plasmas leading to a nearly force-free state. Let us remark that one can construct high β force-free equilibria by adding a homogeneous plasma pressure $\nabla P = 0$ (or a barometric density distribution $\nabla P = -\rho \nabla \Psi$ for configurations with gravity) to any exact force-free configuration. Here we do not study such singular cases, but more realistic configurations where $\nabla P \propto \frac{P}{l}$, where l is a typical length scale of the problem. The equilibrium MHS-1 allows us to compute configurations with different plasma β by prescribing the parameter a_0 , where $a_0 = 0$ corresponds to an exact force-free state. We use our code to investigate how well a magnetic field configuration can be reconstructed by the force-free approach. We start all reconstruction runs with a potential field solution $c = 0.0$ and the magnetic field boundary conditions extracted from the exact solution (artificial vector magnetograms). The configurations in the left hand side in table II have been reconstructed by the assumption of a force-free configuration and the configurations in the right hand side in table II are reconstructed as MHS-equilibria. The force-free reconstruction needs the boundary magnetic field data as input and the MHS-reconstruction additionally requires the plasma-density structure, which we extract here from the analytical solution. This corresponds to artificial tomographic information.

We diagnose the quantities L (L_{FF} for ForceFree and L_{MHS} for MagnetoHydroStatic) and the deviation from the the analytic solution (Error_{FF} for ForceFree and $\text{Error}_{\text{MHS}}$ for MagnetoHydroStatic) similarly as described in the previous sections. For MHS-reconstruction our code finds the magnetic field structure for all configurations with an error corresponding to the discretisation error. If we restrict our code to an exact force-free reconstruction we still get a considerable good agreement with the exact solution for a plasma β of less than 10^{-3} . For higher values of β both the value of L (where $L = 0$ corresponds to an exact force-free state) and the error in the magnetic field increases. Consequently our code finds the expected result that the effect of plasma pressure is negligible for low β configurations. The result also shows that a direct consideration of tomographic information regarding the electron density is only useful for finite β plasmas. For low β plasmas the magnetic field structure is practically not influenced by the plasma density distribution. Let us remark that it is still possible

to consider some indirect information provided by the plasma density for low β plasmas, e.g. the fact that the density gradient parallel to the magnetic field is much lower than the density gradient perpendicular to the magnetic field. Consequently the magnetic field lines are outlined by the emitting plasma. This allows to consider stereoscopic information for the reconstruction of low β plasmas (Wiegelmann and Neukirch, 2002).

3.4. SPEED OF THE METHOD

The speed of our code is approximately proportional to N^5 (N is the number of points for one side of the computational box) similar as found by (Wheatland et al., 2000) for the force-free case. This N^5 dependence looks discouraging for the reconstruction of large boxes. We undertake some rough estimations if the method is practical for modern vector magnetographs. For a grid of $N=40$ a reconstruction takes about 5 min on a 4 processor computer. The IVM vector magnetograph in Hawaii has a resolution of $N=256$ pixel. Consequently a reconstruction with full IVM-resolution would take approximately $5\text{min} \cdot (256/40)^5 \approx 35\text{days}$. If only the half IVM-resolution is used the reconstruction time would be $5\text{min} \cdot (128/40)^5 \approx 28\text{hours}$, which seems to be acceptable. We are optimistic that an improved numerical scheme (e.g. using conjugated gradients or multi-grid methods), a massive parallelization (Using 16-32 processors instead of 4.¹) and increasing computer speed will speed up the reconstruction time significantly. The computing time for the optimization approach seems to be high, but comparisons of the optimization method with classical MHD relaxation (for the force-free case) have shown that the optimization method is more effective (Wiegelmann and Neukirch, 2003). Direct extrapolation methods (e.g. (Wu, Chang, and Hagyard, 1985)) are much faster than iterative methods but known to become unstable with increasing coronal height.

4. Using coronal magnetic field information as a constraint for tomography

Until now, we used information regarding the coronal density and pressure structure as given. In principal we could consider density and pressure in functional (4) as additional variables to be optimized just as \mathbf{B} . In this case, however, the problem of minimizing L would be

¹ The method seems to parallelize quite well. On 4 processors the reconstruction is about 3 times faster than on one processor.

Table II. force-free and MHS-reconstruction. The first column contains the plasma β , the second column a_0 , the third column the final value of L for a force-free reconstruction, the fourth column the error in the magnetic field structure compared to the analytic solution, the fifth column the final L -value for a MHS-reconstruction and finally the sixth column the error in the magnetic field structure compared to the analytic solution for the MHS-reconstruction. All runs have been computed with MHS-1 on a grid $n_x = n_y = 40$, $n_z = 20$ for 5000 iteration steps.

Plasma β	a_0	L_{FF}	Error _{FF}	L_{MHS}	Error _{MHS}
0	0	0.027	$1.5 \cdot 10^{-5}$		
10^{-4}	0.00045	0.028	$1.5 \cdot 10^{-5}$	0.028	$1.5 \cdot 10^{-5}$
10^{-3}	0.0045	0.04	$1.5 \cdot 10^{-4}$	0.028	$1.5 \cdot 10^{-5}$
10^{-2}	0.045	1.26	$4.9 \cdot 10^{-4}$	0.028	$1.5 \cdot 10^{-5}$
10^{-1}	0.41	112	$6.0 \cdot 10^{-3}$	0.027	$1.7 \cdot 10^{-5}$
0.2	0.74	807	0.05	0.015	$1.0 \cdot 10^{-5}$
0.3	1.0	1443	0.2	0.007	$2.0 \cdot 10^{-6}$

hopelessly underdetermined even if the boundary values of \mathbf{B} , ρ and P were given at the Sun's surface.

If the magnetic field was known on the other hand, we could use (4) and assume a temperature variation to determine a consistent density and pressure. Even though we will find immediately that this approach is doomed to fail we here mention for completeness the optimization equations which can be derived from (4)

$$\rho = mN, \quad P = k_B T N$$

and we get (see the appendix B)

$$\frac{1}{2} \frac{dL}{dt} = \int_V H \frac{\partial N}{\partial t} d^3x + \int_S I \frac{\partial N}{\partial t} d^2x, \quad (24)$$

$$H = \mu_0 m \boldsymbol{\Omega}_{\mathbf{a}} \cdot \nabla \Psi - \mu_0 k_B T \nabla \cdot \boldsymbol{\Omega}_{\mathbf{a}}, \quad (25)$$

$$I = \mu_0 k_B T \boldsymbol{\Omega}_{\mathbf{a}} \cdot \hat{\mathbf{n}}. \quad (26)$$

(See (8) for the definition of $\boldsymbol{\Omega}_{\mathbf{a}}$ and $\boldsymbol{\Omega}_{\mathbf{b}}$.)² Physically speaking, the solution to these equations yield a pressure which exactly balances ex-

² Let us remark that the general form of $\frac{dL}{dt}$ will vary both the density distribution and the magnetic field

$$\frac{1}{2} \frac{dL}{dt} = - \int_V \frac{\partial \mathbf{B}}{\partial t} \cdot \mathbf{F} + H \frac{\partial N}{\partial t} d^3x - \int_S \frac{\partial \mathbf{B}}{\partial t} \cdot \mathbf{G} + I \frac{\partial N}{\partial t} d^2x.$$

cessive magnetic field forces onto the plasma. However, due to the small value of β in the corona, already a small relative error in the assumed magnetic field will result in residual forces which need a huge plasma pressure to be balanced so that a small relative error in \mathbf{B} will produce a large relative error in N . We obviously need another approach to get hold of a decent estimate of the coronal density distribution and this must be based on additional observations.

The coronal electron density can be observed by coronagraphs. Unfortunately, coronagraphs yield only integrated column densities along the line-of-sight and the 3D density distribution itself has to be reconstructed from these measurements by means of a tomographic inversion (Zidowitz, 1999; Frazin, 2000; Frazin, 2002). This inversion process has besides its intrinsic ill-posedness additional problems to cope with if applied to coronagraph data:

- non-stationarity of the coronal density structures,
- incomplete data due to the occultation of the image centers (exterior tomography problem),
- non-ideal viewing geometry due to the tilt of the Sun's axis with respect to the ecliptic.

As a result of all these problems, the spatial resolution which ultimately can be achieved with the reconstruction is limited. The conventional procedure to obtain a reliable solution is to minimize an expression of the following form:

$$G(N) = \sum_{p,i} |I_{p,i}^{\text{obs}} - \mathcal{I}_{p,i}(N)|^2 + \mu \int_V |R(N)|^2 d^3x, \quad (27)$$

where $I_{p,i}^{\text{obs}}$ is the observed intensity in pixel p of image i and $\mathcal{I}_{p,i}$ is the respective simulated intensity which is calculated from a density N as a line-of-sight integral

$$\mathcal{I}_{p,i} = \int_{\mathcal{C}_{p,i}} N d\ell. \quad (28)$$

Here, $\mathcal{C}_{p,i}$ is the beam from pixel p of image i , i.e. the location of points $\in V$ which project onto the respective pixel. We omit here modifications of (28) due to the scattering geometry and the scattering crosssection of the electrons which lead to slight variations of the integrand in (28). In (27), R is a regularization function to be specified below. The primary aim is to find a density model N which makes the first term vanish. In this case N is compatible with the observations. However, due to measurements errors, inconsistencies of the observations mentioned above and its possible insensitivity to certain density structures, it does not make sense to minimize the first term alone below a level approximately given by

the measurement error variance. To stabilize the model reconstruction on density structures to which the observations are insensitive, the regularization term is added with a regularization parameter μ tuned so that the first term is approximately brought down to the observation error variance when the complete expression G is minimal.

Since $\mathcal{I}(N)$ is basically an integration operator, $R(N)$ very often is chosen as a differential operator, e.g.,

$$R(N) = \nabla^2 N \quad (29)$$

As a result, while the integration makes $\mathcal{I}(N)$ insensitive to small scale structures, $R(N)$ responds to these but has little effect on the large scales. Therefore, when minimizing G , the large scales are shaped by the first term to comply with the observations, while the small scales are kept smooth by the regularization term in G . The transition between large and small scales is mainly determined by the weight μ of the regularization in G which must be enhanced the worse the quality of the observations. In this sense, the spatial resolution of the model density N which can be achieved depends largely on errors, inconsistencies and gaps of the data.

But the power of the regularization term goes beyond suppressing unwanted small scale noise in the reconstructed model N . Any additional physical constraint for N can be included here just like the $\nabla \cdot \mathbf{B} = 0$ constraint was added to the force balance condition in (4). One obvious constraint for the density is its positivity, which can be taken account of in R by so-called barrier functions (see (Frazin, 2000)). For a more stabilizing constraint we may return to (24). It was derived so as to minimize the square of $\Omega_{\mathbf{a}}$ which is proportional to the local force balance. Note that $\Omega_{\mathbf{b}}$ has no dependence on N and therefore is not varied here. The argument which led us to discard (24) as a starting point for an iteration for the density mainly applies to the force components $\Omega_{\mathbf{a}\perp} \propto (\nabla \times \mathbf{B}) \times \mathbf{B} - \mu_0(\nabla_{\perp} P + \rho \nabla_{\perp} \Psi)$ perpendicular the magnetic field which are dominated by the magnetic term to lowest order. We therefore choose a regularization term which at least takes care of the field-aligned force balance in $\Omega_{\mathbf{a}\parallel} \propto -\mu_0(\nabla_{\parallel} P + \rho \nabla_{\parallel} \Psi)$. This is achieved by

$$R(N) = \frac{1}{k_B T} (\hat{\mathbf{B}} \cdot \nabla) P + \rho (\hat{\mathbf{B}} \cdot \nabla) \Psi = (\hat{\mathbf{B}} \cdot \nabla) N - \frac{\hat{\mathbf{B}} \cdot \hat{\mathbf{r}}}{H_0} N, \quad (30)$$

where again an isothermal plasma is assumed and H_0 is the pressure scale height of the solar corona as in (20). An extension to a varying temperature is straight forward if it is given, however we cannot solve for an unknown T unless we make use of additional observations.

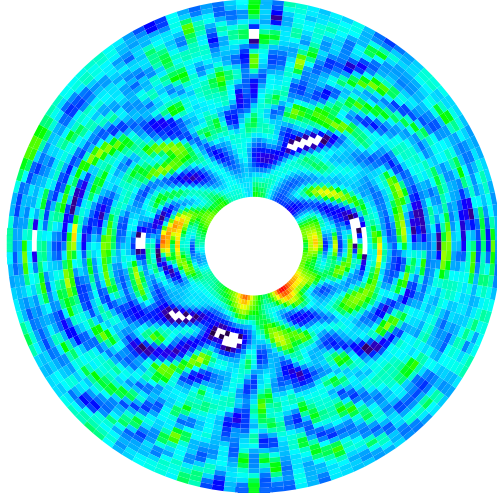


Figure 5. A reconstruction of completely noisy images with the regularization term (30). The visible structures are imprints of the dipole magnetic field assumed in the regularization term.

The regularization term (30) effectively smoothes the density out along the magnetic field lines and thereby takes account of the fact that the transport coefficients in a magnetized plasma are much larger along the magnetic field than in perpendicular direction. In perpendicular direction to $\hat{\mathbf{B}}$ the density may have gradients as sharp as our model resolution allows without changing the value of G .

The magnetic field assumed in the test calculations below was a simple dipole field. The effect of the above regularization operator becomes particularly visible if instead of meaningful data, we assume that I^{obs} is pure noise. The magnetic field then is the only real information in the inversion process and it becomes directly visible in the reconstruction results (see Fig 5).

In appendix C we derive an expression for an iterative descent step analogous to (24) but which is preferable to (24) because it includes the additional observations to stabilize the reconstruction

$$\frac{dG}{dt} = \int_V H \frac{\partial N}{\partial t} d^3x + \int_S I \frac{\partial N}{\partial t} d^2x, \quad (31)$$

where

$$\begin{aligned} H(\mathbf{x}) = & 2 \sum_{p,i} \delta_{C_{p,i}}(\mathbf{x}) (\mathcal{I}_{p,i}(N) - I_{p,i}^{\text{obs}}) \\ & - 2\mu[(\hat{\mathbf{B}} \cdot \nabla)R(N) + \frac{\hat{\mathbf{B}} \cdot \hat{\mathbf{r}}}{H_0}R(N)], \end{aligned} \quad (32)$$

$$I(\mathbf{x}) = 2\mu(\hat{\mathbf{B}} \cdot \hat{\mathbf{n}})R(N) \quad (33)$$

and $\delta_{C_{p,i}}$ is 1 inside the beam emanating from pixel p of image i and 0 otherwise (see appendix C).

In order to test the feasibility of our scheme, we minimize (31) for a 2D test model by means of a conjugate gradient iteration. In table III we compare the action of this operator with more conventional means of regularization for a two-dimensional reconstruction. Here, the model and data errors of a reconstructed model density N are defined as

$$\begin{aligned} \text{data error} &= \frac{1}{2} \sum_{p,i} |I_{p,i}^{\text{obs}} - \mathcal{I}_{p,i}(N)|^2, \\ \text{model error} &= \frac{1}{2} \int_V |N_{\text{ana}} - N|^2 d^3x. \end{aligned}$$

Here, N_{ana} is the analytic density model used to obtain the data I^{obs} . The reconstruction a) was obtained without explicit regularization (i.e. with $\mu = 0$). Instead, the iteration was stopped after 13 iterations when the model error was minimal. Subsequent iterations further decrease the data error but enhance the model error (which for real data is not known), a phenomenon which is known as semiconvergence. For reconstructions b) and d) the conventional regularization operator (29), for c) and e) the operator (30) was used, however with the scale height H_0 set to ∞ .

In cases d) and e), the regularization parameter μ and the number of iterations were optimized to achieve the best agreement with the original model. We show these results only to demonstrate how close a reconstruction can come to the true solution in principle. In practical cases, however, the true density distribution is not known and the optimum solution has to be sought based only on the values for the data error and the regularization term. In cases b) and c) these values have been used in an L-curve search for the optimum solution (Hansen and O’Leary, 1993).

In Fig. 6 we show the models associated with the test inversions in table III. The upper left shows the original model simulating a coronal loop on the western limb and a streamer on the eastern limb. This model was used to calculate the artificial data used as input for the reconstruction after some noise was added. The standard deviation of the noise was $3 \cdot 10^{-2}$ times the square root of the local data intensity when the maximum data intensity is normalized to unity.

In terms of the model error, (30) yields slightly better results than (29). The major improvement comes from the region close to the occulter. In this region conventional tomography can only yield a limited

Table III. Comparison of different regularization methods. The model and data errors are defined in the text. The results a) to c) correspond to the cases in Fig. 6. Case a) uses no regularization at all and has a minimum model error after 14 iteration steps. Cases b) and d) use the isotropic regularization as in (29), cases c) and e) the isotropic regularization as in (29). Iteration steps and μ are optimized in b) and c) from an L-curve search, in cases d) and e) for a minimum model error.)

Regularization method	optimal iteration steps	model error	data error
a) stopping rule, $R=0$	14	12.4	$6.46 \cdot 10^{-5}$
b) $R=(29)$, $\mu=0.01082$	102	1.65	$13.9 \cdot 10^{-5}$
c) $R=(30)$, $\mu=0.00787$	103	1.21	$12.5 \cdot 10^{-5}$
d) $R=(29)$, $\mu=0.0050$	53	1.21	$12.2 \cdot 10^{-5}$
e) $R=(30)$, $\mu=0.0065$	120	1.13	$12.0 \cdot 10^{-5}$

resolution because close to the occulter the structures are only seen in few observations. On the other hand, this is the area where we observe the strongest gradients in the density structures and where spatial resolution is needed most. This fundamental lack of resolution can only be overcome if new information (either observations or assumptions) is fed into the inversion process. The new regularization operator (30) contains this additional information in form of the local magnetic field direction.

The price we have to pay is a more lengthy computation as the number of iterations increases (see Table III). Another problem which might occur are spurious field-aligned density structures in the reconstruction which add up to zero in the tomographic projections. Formally, (30) has a nullspace which asymptotically comes close to the nullspace of the \mathcal{I} . In practical cases, however, the discretization error in the differentiation is sufficient to give (30) some isotropic component so that even exactly field-aligned structures yield a small non-zero contribution in a discretized operator (30).

5. Conclusions

In this paper we undertook a first step towards the inclusion of tomographic information into the reconstruction of coronal magnetic fields and a first step towards the inclusion of coronal magnetic field information into the tomographic inversion procedure. Until now we

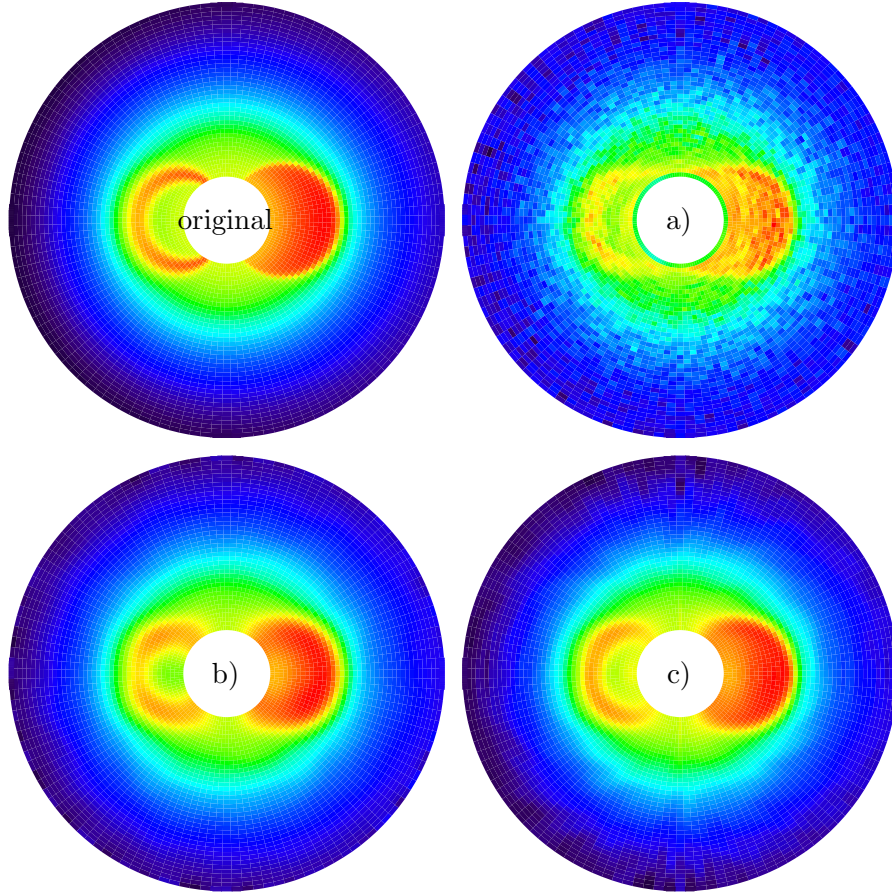


Figure 6. Comparison of different regularization methods for the reconstruction of the original model N_{ana} in the upper left. The results a) to c) correspond to the cases in table III.

considered the reconstruction of the magnetic field from its boundary values with an optimization code when the density structure is given and the tomographic reconstruction of the coronal density distribution from coronagraph data under the constraint of a given magnetic field. As neither N and nor \mathbf{B} are known a priori in the solar corona, we rather have to find a way to consistently reconstruct both quantities from the observations simultaneously without the assumption that one of the quantities is given.

In fact we observe that the two approaches discussed in the previous sections are not only formally closely related but can be derived from a single variational problem if the expression for L is slightly modified

and the factor B^{-2} in the integrand is omitted

$$\begin{aligned}
L(\mathbf{B}, N) = & \int_V |(\nabla \times \mathbf{B}) \times \mathbf{B} - \mu_0(\nabla P + \rho \nabla \Psi)|^2 + B^2 |\nabla \cdot \mathbf{B}|^2 d^3x \\
& + \frac{1}{\mu'} \sum_{p,i} |I_{p,i}^{\text{obs}} - \mathcal{I}_{p,i}(N)|^2.
\end{aligned} \tag{34}$$

A variation with respect to \mathbf{B} obviously leads to an iteration scheme similar to (5), except for the effect of the B^{-2} term in the integrand. We have tested the resulting scheme and found that it also converges towards the analytic solution from which the boundary conditions were taken, but the convergence speed was much slower than with (5). If L is varied with respect to N alone, we can ignore the terms which depend only on \mathbf{B} and we obtain (31) again if we discard the perpendicular force balance in $\Omega_{\mathbf{a}}$. This suggests that the individual reconstruction problems for \mathbf{B} and N are just two projections of a unique reconstruction problem. In this case we could apply both algorithms simultaneously and replace N in the algorithm for \mathbf{B} and \mathbf{B} in the algorithm for N by the respective iterate and the problem as a whole should converge as they do individually. A test of this hypothesis will be attempted in the future. The code is planned for use within the STEREO mission.

Acknowledgements

The authors thank Thomas Neukirch for useful discussions. This work was supported by DLR-grant 50 OC 0007. We thank an unknown referee for useful comments.

Appendix

A. Derivation of \mathbf{F} and \mathbf{G} in (5).

(4) can also be written as

$$L = \int_V B^2 (\Omega_a^2 + \Omega_b^2) d^3x. \tag{A.1}$$

$$\begin{aligned}
\Omega_{\mathbf{a}} &= B^{-2} [(\nabla \times \mathbf{B}) \times \mathbf{B} + \mathbf{u}] \\
\Omega_{\mathbf{b}} &= B^{-2} [(\nabla \cdot \mathbf{B}) \mathbf{B}] \\
\mathbf{u} &= -\mu_0(\nabla P + \rho \nabla \Psi)
\end{aligned} \tag{A.2}$$

We vary L with respect to an iteration parameter t and get

$$\begin{aligned} \frac{1}{2} \frac{dL}{dt} &= \int_V \boldsymbol{\Omega}_a \cdot \frac{\partial}{\partial t} [(\nabla \times \mathbf{B}) \times \mathbf{B} + \mathbf{u}] d^3x \\ &+ \int_V \boldsymbol{\Omega}_b \cdot \frac{\partial}{\partial t} [(\nabla \cdot \mathbf{B}) \mathbf{B}] d^3x \\ &- \int_V (\Omega_a^2 + \Omega_b^2) \mathbf{B} \cdot \frac{\partial \mathbf{B}}{\partial t} d^3x. \end{aligned} \quad (\text{A.3})$$

Our aim is now to use vector identities and Gauss law in such way that all terms contain a product with $\frac{\partial \mathbf{B}}{\partial t}$. This will allow us to provide explicit evolution equations for \mathbf{B} to minimize L . The third term has the correct form already. We expand the first and second term

$$\begin{aligned} \Rightarrow \frac{1}{2} \frac{dL}{dt} &= \int_V \boldsymbol{\Omega}_a \cdot \left[\left(\nabla \times \frac{\partial \mathbf{B}}{\partial t} \right) \times \mathbf{B} \right] d^3x \\ &+ \int_V \boldsymbol{\Omega}_a \cdot \left[(\nabla \times \mathbf{B}) \times \frac{\partial \mathbf{B}}{\partial t} \right] d^3x \\ &+ \int_V \boldsymbol{\Omega}_b \cdot \left[\left(\nabla \cdot \frac{\partial \mathbf{B}}{\partial t} \right) \mathbf{B} \right] d^3x \\ &+ \int_V \boldsymbol{\Omega}_b \cdot \left[(\nabla \cdot \mathbf{B}) \frac{\partial \mathbf{B}}{\partial t} \right] d^3x \\ &- \int_V (\Omega_a^2 + \Omega_b^2) \mathbf{B} \cdot \frac{\partial \mathbf{B}}{\partial t} d^3x. \end{aligned} \quad (\text{A.4})$$

The fourth and fifth term have the correct form. We apply the vector identities $\mathbf{a} \cdot (\mathbf{b} \times \mathbf{c}) = \mathbf{b} \cdot (\mathbf{c} \times \mathbf{a}) = \mathbf{c} \cdot (\mathbf{a} \times \mathbf{b})$ to the first and second term

$$\begin{aligned} \Rightarrow \frac{1}{2} \frac{dL}{dt} &= \int_V \left(\nabla \times \frac{\partial \mathbf{B}}{\partial t} \right) \cdot (\mathbf{B} \times \boldsymbol{\Omega}_a) d^3x \\ &+ \int_V \frac{\partial \mathbf{B}}{\partial t} \cdot (\boldsymbol{\Omega}_a \times (\nabla \times \mathbf{B})) d^3x \\ &+ \int_V (\boldsymbol{\Omega}_b \cdot \mathbf{B}) \nabla \cdot \frac{\partial \mathbf{B}}{\partial t} d^3x \\ &+ \int_V [\boldsymbol{\Omega}_b (\nabla \cdot \mathbf{B})] \cdot \frac{\partial \mathbf{B}}{\partial t} d^3x \\ &- \int_V (\Omega_a^2 + \Omega_b^2) \mathbf{B} \cdot \frac{\partial \mathbf{B}}{\partial t} d^3x. \end{aligned} \quad (\text{A.5})$$

Term two, four and five have the correct form. We apply $(\nabla \times \mathbf{a}) \cdot \mathbf{b} = \mathbf{a} \cdot (\nabla \times \mathbf{b}) + \nabla \cdot (\mathbf{a} \times \mathbf{b})$ to term 1 and $\psi \nabla \cdot \mathbf{a} = -\mathbf{a} \cdot \nabla \psi + \nabla \cdot (\mathbf{a} \psi)$ to term 3

$$\Rightarrow \frac{1}{2} \frac{dL}{dt} = - \int_V \frac{\partial \mathbf{B}}{\partial t} \cdot [\nabla \times (\boldsymbol{\Omega}_a \times \mathbf{B})] d^3x$$

$$\begin{aligned}
& - \int_V \nabla \cdot \left[(\boldsymbol{\Omega}_a \times \mathbf{B}) \times \frac{\partial \mathbf{B}}{\partial t} \right] d^3x \\
& + \int_V \frac{\partial \mathbf{B}}{\partial t} \cdot (\boldsymbol{\Omega}_a \times (\nabla \times \mathbf{B})) d^3x \\
& - \int_V \nabla(\boldsymbol{\Omega}_b \cdot \mathbf{B}) \cdot \frac{\partial \mathbf{B}}{\partial t} d^3x \\
& + \int_V \nabla \cdot \left[(\boldsymbol{\Omega}_b \cdot \mathbf{B}) \frac{\partial \mathbf{B}}{\partial t} \right] d^3x \\
& + \int_V [\boldsymbol{\Omega}_b (\nabla \cdot \mathbf{B})] \cdot \frac{\partial \mathbf{B}}{\partial t} d^3x \\
& - \int_V (\Omega_a^2 + \Omega_b^2) \mathbf{B} \cdot \frac{\partial \mathbf{B}}{\partial t} d^3x. \tag{A.6}
\end{aligned}$$

Term one, three, four, six and seven have the correct form. We apply Gauss law to term two and five

$$\begin{aligned}
\Rightarrow \frac{1}{2} \frac{dL}{dt} &= - \int_V \frac{\partial \mathbf{B}}{\partial t} \cdot [\nabla \times (\boldsymbol{\Omega}_a \times \mathbf{B})] d^3x \\
& - \int_S \hat{\mathbf{n}} \cdot \left[(\boldsymbol{\Omega}_a \times \mathbf{B}) \times \frac{\partial \mathbf{B}}{\partial t} \right] d^2x \\
& + \int_V \frac{\partial \mathbf{B}}{\partial t} \cdot (\boldsymbol{\Omega}_a \times (\nabla \times \mathbf{B})) d^3x \\
& - \int_V \nabla(\boldsymbol{\Omega}_b \cdot \mathbf{B}) \cdot \frac{\partial \mathbf{B}}{\partial t} d^3x \\
& + \int_S \hat{\mathbf{n}}(\boldsymbol{\Omega}_b \cdot \mathbf{B}) \cdot \frac{\partial \mathbf{B}}{\partial t} d^2x \\
& + \int_V [\boldsymbol{\Omega}_b (\nabla \cdot \mathbf{B})] \cdot \frac{\partial \mathbf{B}}{\partial t} d^3x \\
& - \int_V (\Omega_a^2 + \Omega_b^2) \mathbf{B} \cdot \frac{\partial \mathbf{B}}{\partial t} d^3x. \tag{A.7}
\end{aligned}$$

Now all terms but the second have the correct form. We apply $\mathbf{a} \cdot (\mathbf{b} \times \mathbf{c}) = \mathbf{c} \cdot (\mathbf{a} \times \mathbf{b})$ to the second term

$$\begin{aligned}
\Rightarrow \frac{1}{2} \frac{dL}{dt} &= - \int_V \frac{\partial \mathbf{B}}{\partial t} \cdot [\nabla \times (\boldsymbol{\Omega}_a \times \mathbf{B})] d^3x \\
& - \int_S [\hat{\mathbf{n}} \times [(\boldsymbol{\Omega}_a \times \mathbf{B})]] \cdot \frac{\partial \mathbf{B}}{\partial t} d^2x \\
& + \int_V \frac{\partial \mathbf{B}}{\partial t} \cdot (\boldsymbol{\Omega}_a \times (\nabla \times \mathbf{B})) d^3x \\
& - \int_V \nabla(\boldsymbol{\Omega}_b \cdot \mathbf{B}) \cdot \frac{\partial \mathbf{B}}{\partial t} d^3x \\
& + \int_S \hat{\mathbf{n}}(\boldsymbol{\Omega}_b \cdot \mathbf{B}) \cdot \frac{\partial \mathbf{B}}{\partial t} d^2x
\end{aligned}$$

$$\begin{aligned}
& + \int_V [\boldsymbol{\Omega}_b (\nabla \cdot \mathbf{B})] \cdot \frac{\partial \mathbf{B}}{\partial t} d^3x \\
& - \int_V (\Omega_a^2 + \Omega_b^2) \mathbf{B} \cdot \frac{\partial \mathbf{B}}{\partial t} d^3x.
\end{aligned} \tag{A.8}$$

Now all terms have the correct form and we write them more compact as

$$\Rightarrow \frac{1}{2} \frac{dL}{dt} = - \int_V \frac{\partial \mathbf{B}}{\partial t} \cdot \mathbf{F} d^3x - \int_S \frac{\partial \mathbf{B}}{\partial t} \cdot \mathbf{G} d^2x, \tag{A.9}$$

with

$$\begin{aligned}
\mathbf{F} = & \nabla \times (\boldsymbol{\Omega}_a \times \mathbf{B}) - \boldsymbol{\Omega}_a \times (\nabla \times \mathbf{B}) \\
& + \nabla (\boldsymbol{\Omega}_b \cdot \mathbf{B}) - \boldsymbol{\Omega}_b (\nabla \cdot \mathbf{B}) + (\Omega_a^2 + \Omega_b^2) \mathbf{B},
\end{aligned} \tag{A.10}$$

$$\mathbf{G} = \hat{\mathbf{n}} \times (\boldsymbol{\Omega}_a \times \mathbf{B}) - \hat{\mathbf{n}} (\boldsymbol{\Omega}_b \cdot \mathbf{B}). \tag{A.11}$$

B. Derivation of H and I in (24).

We vary L with respect to an iteration parameter t where the magnetic field is independent from t here.

$$\frac{1}{2} \frac{dL}{dt} = \int_V \boldsymbol{\Omega}_a \cdot \frac{\partial}{\partial t} [(\nabla \times \mathbf{B}) \times \mathbf{B} - \mu_0 (\nabla P + \rho \nabla \Psi)] d^3x \tag{B.1}$$

We write the pressure P and the mass density ρ as functions of the number density N

$$\begin{aligned}
\Rightarrow \frac{1}{2} \frac{dL}{dt} = & \int_V \boldsymbol{\Omega}_a \cdot \frac{\partial}{\partial t} [(\nabla \times \mathbf{B}) \times \mathbf{B} \\
& - \mu_0 (k_B T \nabla N + m N \nabla \Psi)] d^3x
\end{aligned} \tag{B.2}$$

Our aim is to write all terms as products with $\frac{\partial N}{\partial t}$ to derive evolution equations for N to minimize L . The first term vanishes here because \mathbf{B} does not depend on t . We expand the second term

$$\begin{aligned}
\Rightarrow \frac{1}{2} \frac{dL}{dt} = & -\mu_0 \int_V \boldsymbol{\Omega}_a \cdot k_B T \nabla \left(\frac{\partial N}{\partial t} \right) d^3x \\
& -\mu_0 \int_V \boldsymbol{\Omega}_a \cdot m \frac{\partial N}{\partial t} \nabla \Psi d^3x.
\end{aligned} \tag{B.3}$$

The second term has the correct form. We apply $\mathbf{a} \cdot \nabla \psi = \nabla \cdot (\mathbf{a} \psi) - \psi \nabla \cdot \mathbf{a}$ to the first term

$$\Rightarrow \frac{1}{2} \frac{dL}{dt} = -\mu_0 \int_V \nabla \cdot \left(\boldsymbol{\Omega}_a k_B T \frac{\partial N}{\partial t} \right) d^3x$$

$$\begin{aligned}
& +\mu_0 \int_V \nabla \cdot \boldsymbol{\Omega}_{\mathbf{a}} k_B T \frac{\partial N}{\partial t} d^3x \\
& -\mu_0 \int_V \boldsymbol{\Omega}_{\mathbf{a}} \cdot m \frac{\partial N}{\partial t} \nabla \Psi d^3x.
\end{aligned} \tag{B.4}$$

Term two and three have the correct form. We apply Gauss law to the first term

$$\begin{aligned}
\Rightarrow \frac{1}{2} \frac{dL}{dt} &= -\mu_0 \int_S \hat{\mathbf{n}} \cdot \boldsymbol{\Omega}_{\mathbf{a}} k_B T \frac{\partial N}{\partial t} d^2x \\
& +\mu_0 \int_V \nabla \cdot \boldsymbol{\Omega}_{\mathbf{a}} k_B T \frac{\partial N}{\partial t} d^3x \\
& -\mu_0 \int_V \boldsymbol{\Omega}_{\mathbf{a}} \cdot m \frac{\partial N}{\partial t} \nabla \Psi d^3x.
\end{aligned} \tag{B.5}$$

Now all terms have the correct form and we write more compact

$$\begin{aligned}
\Rightarrow \frac{1}{2} \frac{dL}{dt} &= -\int_V H \frac{\partial N}{\partial t} d^3x - \int_S I \frac{\partial N}{\partial t} d^2x \\
H &= \mu_0 m \boldsymbol{\Omega}_{\mathbf{a}} \cdot \nabla \Psi - \mu_0 k_B T \nabla \cdot \boldsymbol{\Omega}_{\mathbf{a}} \\
I &= \mu_0 k_B T \boldsymbol{\Omega}_{\mathbf{a}} \cdot \hat{\mathbf{n}}.
\end{aligned} \tag{B.6}$$

C. Derivation of H and I in (31).

An essential advantage in the derivation of the variational derivative of G in (27) is the fact that G is convex quadratic expression. While I^{obs} is just a data vector, \mathcal{I} is a linear operator from the model space $\{N(V)\}$ into the data space $\{I_{p,i}\}$:

$$\mathcal{I}_{p,i}(N) = \int_{\mathcal{C}_{p,i}} N(\mathbf{x}) d\ell \quad : \quad \text{model space} \longrightarrow \text{data space}. \tag{C.1}$$

The beam was defined in the main text as $\mathcal{C}_{p,i} = \{\mathbf{x} \in V \mid \mathbf{x} \text{ projects onto pixel } p \text{ for the view direction of image } i\}$. The adjoint of (C.1) is

$$\mathcal{J}(\mathbf{x}, I) = \sum_{p,i} \delta_{\mathcal{C}_{p,i}}(\mathbf{x}) I_{p,i} \quad : \quad \text{data space} \longrightarrow \text{model space}, \tag{C.2}$$

where $\delta_{\mathcal{C}_{p,i}}(\mathbf{x}) = 1$ for $\mathbf{x} \in \mathcal{C}_{p,i}$ and $\delta_{\mathcal{C}_{p,i}} = 0$ else. The adjointness can easily be checked by insertion of the respective definitions into

$$\sum_{p,i} I_{p,i} \mathcal{I}_{p,i}(N) = \int_V \mathcal{J}(\mathbf{x}, I) N(\mathbf{x}) d^3x \tag{C.3}$$

Now minimizing (27)

$$G(N) = \sum_{p,i} |I_{p,i}^{\text{obs}} - \mathcal{I}_{p,i}(N)|^2 + \mu \int_V R(N)^2 d^3x \quad (\text{C.4})$$

with (30)

$$R(N) = \frac{1}{k_B T} (\hat{\mathbf{B}} \cdot \nabla) P + \rho (\hat{\mathbf{B}} \cdot \nabla) \Psi = (\hat{\mathbf{B}} \cdot \nabla) N - \frac{\hat{\mathbf{B}} \cdot \hat{\mathbf{r}}}{H_0} N \quad (\text{C.5})$$

yields

$$\begin{aligned} \frac{dG}{dt} &= 2 \sum_{p,i} (\mathcal{I}_{p,i}(N) - I_{p,i}^{\text{obs}}) \mathcal{I}_{p,i} \left(\frac{\partial N}{\partial t} \right) \\ &+ 2\mu \int_V R \left[(\hat{\mathbf{B}} \cdot \nabla) \frac{\partial N}{\partial t} - \frac{\hat{\mathbf{B}} \cdot \hat{\mathbf{r}}}{H_0} \frac{\partial N}{\partial t} \right] d^3x \\ &= 2 \int_V \mathcal{J}(\mathbf{x}, \mathcal{I}_{p,i}(N) - I_{p,i}^{\text{obs}}) \frac{\partial N}{\partial t} \\ &- 2\mu \int_V \left[(\hat{\mathbf{B}} \cdot \nabla) R + R \frac{\hat{\mathbf{B}} \cdot \hat{\mathbf{r}}}{H_0} \right] \frac{\partial N}{\partial t} d^3x \\ &+ 2\mu \int_S R (\hat{\mathbf{B}} \cdot \hat{\mathbf{n}}) \frac{\partial N}{\partial t} d^2x \\ &= \int_V H \frac{\partial N}{\partial t} d^3x + \int_S I \frac{\partial N}{\partial t} d^2x, \end{aligned}$$

where $\hat{\mathbf{n}}$ is the unit normal on the surface S and

$$\begin{aligned} H(\mathbf{x}) &= 2 \sum_{p,i} \delta_{\mathcal{C}_{p,i}}(\mathbf{x}) (\mathcal{I}_{p,i}(N) - I_{p,i}^{\text{obs}}) \\ &- 2\mu \left[(\hat{\mathbf{B}} \cdot \nabla) R(N) + \frac{\hat{\mathbf{B}} \cdot \hat{\mathbf{r}}}{H_0} R(N) \right], \end{aligned} \quad (\text{C.6})$$

$$I(\mathbf{x}) = 2\mu (\hat{\mathbf{B}} \cdot \hat{\mathbf{n}}) R(N). \quad (\text{C.7})$$

References

- Amari, T., Aly, J.J., Luciani, J.F., Boulmezaoud, T.Z., Mikic, Z.: 1997, *Solar Phys.* **174**, 129.
 Chiu, Y.T., Hilton, H.H.: 1977, *Astrophys. J.* **212**, 821.
 Davila, J.M.: 1994, *Astrophys. J.*, **423**, 871.

- Frazin, R.A.: 2000, *Astrophys. J.*, **530**, 1026.
- Frazin, R.A.: 2002, *Astrophys. J.*, **570**, 408.
- Gary, G.A.: 1989, *Astrophys. J. Suppl.* **69**, 323.
- Geiger, G. and Kanzow, C.: 1999, *Numerische Verfahren zur Loesung unrestringierter Optimierungsaufgaben*, Springer-Verlag.
- Lothian, R.M. and Browning, P.K.: 1995, *Solar Phys.* **161**, 289.
- Louis, A.K.: 1989, *Inverse und schlecht gestellte Probleme*, Teubner Studienbuecher ISBN 3-519-02085-X.
- McClymont, A.N., Jiao, L., Mikic, Z.: 1997, *Solar Phys.* **174**, 191.
- Nakagawa, Y. and Raadu, M.A.: 1972, *Solar Phys.* **25**, 127.
- Petrie, G.J.D. and Neukirch, T.: 2000, *Astron. Astrophys.* **356**, 735.
- Roumeliotis, G.: 1996, *Astrophys. J.* **473**, 1095.
- Rudenko, G.V.: 2001a, *Solar Phys.* **198**, 5.
- Rudenko, G.V.: 2001b, *Solar Phys.* **198**, 279.
- Sakurai, T.: 1981, *Solar Phys.* **69**, 343.
- Sakurai, T.: 1982, *Solar Phys.* **76**, 301.
- Schatten, K.H., Wilcox, J.M., and Ness N.F.: 1969, *Solar Phys.* **6**, 442.
- Schindler, K.: 1972, in McCormac (eds.), *Earth's Magnetospheric Processes* D. Reidel Publ. Comp., Dordrecht 1972, S. 200
- Schmidt, H.V.: 1964 in W.N. Ness (ed.), *ASS-NASA Symposium on the Physics of Solar Flares*, NASA SP-50, p. 107.
- Seehafer, N.: 1978, *Solar Phys.*, **58**, 215.
- Semel, M.: 1967, *Ann. Astrophys.* **30**, 513.
- Semel, M.: 1988, *Astron. Astrophys.* **198**, 293.
- Wiegmann, T., Schindler, K. and Neukirch, T.: 1998, *Solar Phys.* **180**, 439.
- Wiegmann, T. and Neukirch, T.: 2002 *Solar Phys.*, **208**, 233-251.
- Wiegmann, T. and Neukirch, T.: 2003, *Nonlinear Processes in Geophysics*, in press.
- Wu, S.T., Chang, H.M., Hagyard, M.J.: 1985, in M.J. Hagyard (ed.), *Measurements of Solar Magnetic Fields*, NASA CP-2374, p. 17.
- Wheatland, M. S., Sturrock, P. A., and Roumeliotis, G.: 2000, *Astrophys. J.*, 540, 1150-1155.
- Yan, Y. and Sakurai, T.: 2000, *Solar Phys.* **195**, 89.
- Zhao, X. and Hoeksema, J.T.: 1993, *Solar Phys.* **143**, 41.
- Zhao, X. and Hoeksema, J.T.: 1994, *Solar Phys.* **151**, 91.
- Zhao, X., Hoeksema, J.T., and Scherrer, P.H.: 2000, *Astrophys. J.* **538**, 932.
- Zidowitz, S.: 1999 *JGR*, **104**, 9727.

Address for Offprints: Kluwer Prepress Department
P.O. Box 990
3300 AZ Dordrecht
The Netherlands

